analytical chemistry

pubs.acs.org/ac Article

Near-Infrared Optical Transducer for Dynamic Imaging of Cerebrospinal Fluid Glucose in Brain Tumor

Siyang Liu, Ye Liu, Zhe Zhang, Xiaodong Wang, Yicheng Yang, Kai Sun, Jiangbo Yu, Daniel T. Chiu, and Changfeng Wu*

Cite This: *Anal. Chem.* 2022, 94, 14265−14272 Read Online

ACCESS | Metrics & More | Article Recommendations | Supporting Information

ABSTRACT: Aberrant cerebral glucose metabolism is related to many brain diseases, especially brain tumor. However, it remains challenging to measure the dynamic changes in cerebral glucose. Here, we developed a near-infrared (NIR) optical transducer to sensitively monitor the glucose variations in cerebrospinal fluid in vivo. The transducer consists of an oxygen-sensitive nanoparticle combined with glucose oxidase (GOx), yielding highly sensitive NIR phosphorescence in response to blood glucose change. We demonstrated long-term continuous glucose monitoring by using the NIR transducer. After subcutaneous implantation, the glucose transducer provides a strong luminescence signal that can continuously monitor blood glucose fluctuations for weeks. By using the NIR emission of the transducer, we further observed abnormal dynamic changes in cerebrospinal fluid glucose and quantitatively assessed cerebral glucose uptake rates in transgenic mice bearing brain tumors. This study provides a promising method for the diagnosis of various metabolic diseases with altered glucose metabolism.

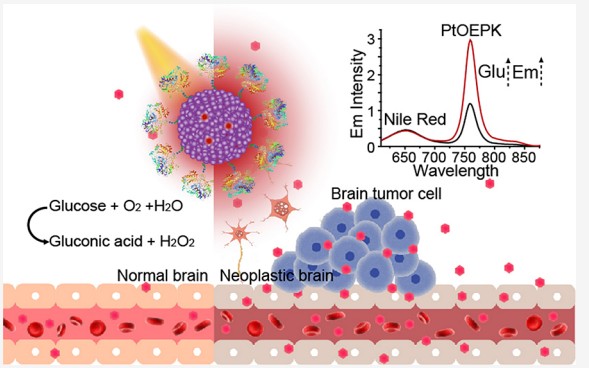

Downloaded via WESTLAKE UNIV on November 28, 2022 at 06:09:25 (UTC).
See https://pubs.acs.org/sharingguidelines for options on how to legitimately share published articles.

INTRODUCTION

Glucose is the primary energy source for most organisms. Aberrant glucose metabolism is associated with many diseases.[1−6] For example, cancer cells exhibit elevated levels of glucose uptake, which has been well established for the prognostic and diagnostic imaging of a variety of cancers. Currently, glucose uptake and metabolism can be assessed clinically by positron emission tomography (PET) using a radioactive glucose analogue, ^{18}F-fluorodeoxyglucose (^{18}F-FDG).[7−11] PET imaging has found wide clinical utility because of its high sensitivity to reveal the metabolic and biochemical functions of diseased organs. Another technique, microdialysis, can be used to measure chemicals such as glucose in the cerebral extracellular fluid.[12] Although this method has the ability to analyze cerebral substances accurately, it requires highly precise operations. In recent years, magnetic resonance imaging (MRI) has been developed for imaging glucose metabolism in vivo.[13] In this technique, radio-frequency pulses are used to fully saturate the hydroxyl protons of glucose, which further affects the signal strength of free water through chemical exchange. Information on glucose or a glucose analogue can be indirectly calculated by detecting the signal of water. MRI has the ability to detect tumor glucose uptake without using radioactive tracers, which has been demonstrated in several disease models, including colorectal tumors, brain tumors, and Alzheimer's disease.[13−16] Despite the progress, it is of great importance to develop new techniques with high sensitivity and a low cost to assess the glucose uptake and metabolism in living organisms.

Optical methods are cost-effective and sensitive for biological detections, and several strategies have been developed for optical glucose sensing and imaging.[17−22] Shibata et al. developed an implantable hydrogel platform based on diboronic acid and a fluorescent dye, which was further immobilized subcutaneously for in vivo continuous glucose monitoring.[23,24] Recently, Maric et al. reported a bioluminescent probe that can accurately measure glucose uptake in living cells and living mice.[25] The bioluminescent probe in tumor xenograft models exhibited high sensitivity that was comparable to the that of the ^{18}F-FDG tracer. Our group developed an optical glucose transducer by combining polymer dots with glucose oxidase for in vivo glucose imaging.[26,27] The long-term monitoring, biocompatibility, and reproducibility of the polymer-dot transducer were further improved with a multienzyme reaction system (glucose oxidase and catalase),

Received: June 17, 2022
Accepted: September 28, 2022
Published: October 7, 2022

© 2022 American Chemical Society

https://doi.org/10.1021/acs.analchem.2c02600
Anal. Chem. 2022, 94, 14265−14272

Scheme 1. Preparation of the Nanoparticle Transducer and the Sensing Mechanism in a Normal Brain and a Neoplastic Brain. (a) Chemical Structures of PSMA, Polystyrene, Nile Red, and PtOEPK and Schematic Illustration of the Preparation of the Nanoparticle Transducer. (b) Detection of Cerebral Glucose Uptake in a Normal Brain and a Neoplastic Brain.

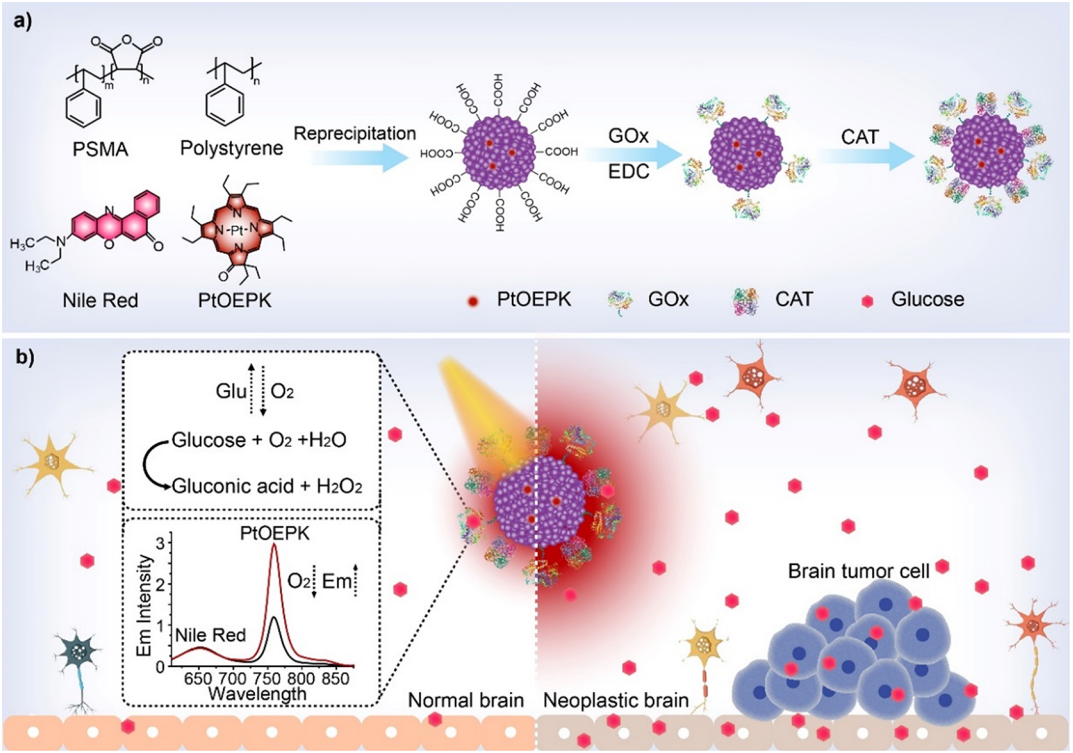

ratiometric calibration, and the hydrogel encapsulation method.[28−30] Moreover, fluorescent glucose analogues have been used for imaging of glucose uptake in astrocytes and neurons by two-photon microscopy.[31] Since glucose is the major neuronal fuel in the brain, many brain diseases are related to altered cerebral glucose metabolism, such as brain tumors,[32] Alzheimer's disease,[16,33] traumatic brain injury,[34−37] and ischemic brain injury.[38] Therefore, it is highly desirable to develop glucose probes with a near-infrared (NIR) emission for glucose detection in the brain.

Here, we report an optical glucose nanoparticle transducer with an NIR emission that enables through-skull monitoring of cerebral glucose uptake in the mouse brain. We used Nile Red and a Pt complex as a Förster resonance energy transfer (FRET) pair in a polymer matrix to construct a ratiometric oxygen-sensitive probe. The polymer nanoparticles were further integrated with glucose oxidase (GOx), resulting in highly sensitive NIR phosphorescence in response to glucose concentration. The glucose transducer not only showed good sensing performance in long-term continuous glucose monitoring but also had the ability to detect abnormal cerebral glucose metabolism and quantify the cerebral glucose uptake rate in transgenic mice with brain tumors. This work provides a promising method for dynamic imaging of cerebrospinal fluid glucose in small animals.

EXPERIMENTAL SECTION

Preparation of Polymer Nanoparticles. In a typical preparation, stock solutions of polystyrene, the functional amphiphilic polymer poly(styrene-*co*-maleic anhydride) (PSMA), Nile Red, and Pt(II) octaethylporphine ketone (PtOEPK) were prepared by dissolving in THF with concentrations of 1000, 1000, 100, and 500 μg/mL, respectively. The polymer and dyes were further diluted and mixed to prepare the precursor solution with polystyrene (100 μg/mL), PSMA (50 μg/mL), Nile Red (5 μg/mL), and PtOEPK (0−10 μg/mL). Then, 1 mL of the precursor solution was added to ultrapure water (10 mL) followed with sonication (120 s). Then, the THF was further removed to obtain nanoparticles.

Bioconjugation. Carboxyl groups were generated on the surface of the nanoparticles after the anhydrides of PSMA were hydrolyzed. NP−GOx−CAT bioconjugates were prepared by using an EDC-catalyzed reaction. The amine groups on GOx and CAT were bioconjugated with the carboxyl groups on the nanoparticles. In this reaction, a HEPES solution (40 μL, 1 mol/L), GOx (40 μL, 10 μM in 20 mM HEPES), and EDC (40 μL, 5 mg/mL in H_2O) were mixed with 2 mL of nanoparticles (100 μg/mL in H_2O). The mixture was mixed on a vortex, and then the catalase enzyme (40 μL, 60 μM in 20 mM HEPES) was added. Then, the mixture was rocked for 2 h at 25 °C to develop the final nanoparticle transducer (NP−GOx−CAT).

In Vivo Glucose Monitoring. The experimental group consisted of three BALB/C mice (6−8 weeks, female). During the experiment, all of the mice were kept warm with a heating bed. After each mouse was anesthetized with isoflurane, 100 μL of a nanoparticle transducer (100 μg/mL) in water solution was directly injected into subcutaneous tissue. After 24 h, the implanted nanoparticle transducer was stabilized as the water was absorbed completely. Since the anesthesia process can cause fluctuations in the blood glucose level, optical imaging was performed after 40 min anesthesia administration. The in vivo images were acquired on an IVIS Lumina III imaging

https://doi.org/10.1021/acs.analchem.2c02600
Anal. Chem. 2022, 94, 14265−14272

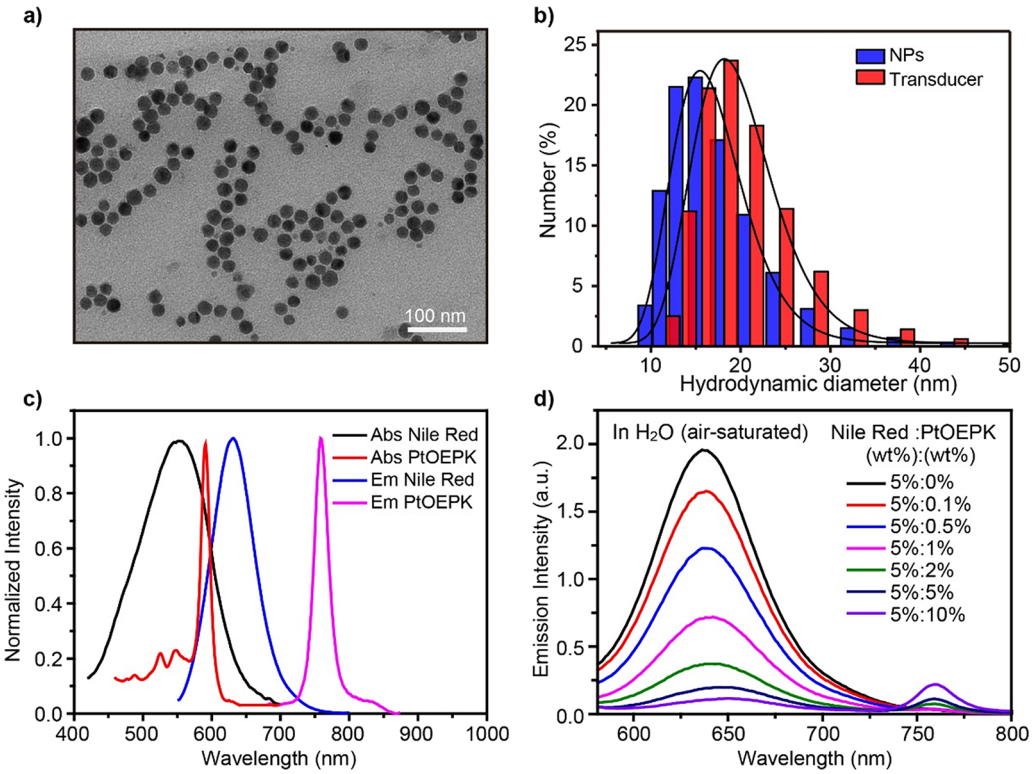

Figure 1. Characterization of the nanoparticles and nanoparticle transducer. (a) TEM image of the as-prepared nanoparticles. (b) Hydrodynamic diameters of the nanoparticles and transducer. The black lines are the lognormal fitting curves of the diameters of the nanoparticles and nanoparticle−GOx transducer. (c) Absorption spectra and emission spectra of Nile Red and PtOEPK. (d) Emission spectra of the nanoparticles doped with a constant Nile Red concentration (5 wt %) and varied PtOEPK concentrations (0−10 wt %) in an air-saturated solution.

system by using emission filters with center wavelengths of 670 and 790 nm and the same bandwidth of 40 nm. Blood samples were collected from the tail after optical imaging. The blood glucose concentration of each mouse was measured by a commercial glucose meter. For the glucose administration, sterilized glucose (150 μL, 1 M in H_2O) was administered by intraperitoneal injection to elevate the blood glucose level. During the process, optical images and concentrations of blood glucose were obtained every 5 min. The control group consisted of three mice without intraperitoneal injection of glucose.

Dynamic Imaging of Cerebral Glucose Uptake. The experimental group included 11 ND2:SmoA1 female mice, and the control group included 11 C57BL/6 mice (6−8 weeks old). The mice were anesthetized with isoflurane, and 2 and 10 μL of the nanoparticle transducer (100 μg/mL) were implanted into the dorsal site and lateral ventricle of the two groups of mice. For intracerebroventricular injection of the nanoparticle transducer, the mice were anesthetized using isoflurane and then immobilized on a stereotaxic apparatus (Shanghai Bio-will Co., Ltd.). The top of the mouse's head was shaved and cleaned with 75% ethanol. After that, a linear skin incision was made over the bregma, and 3% hydrogen peroxide was applied to remove the periost over the bregma. Then, a burr hole was drilled on the left side of the skull using a cranial drill (bregma, −0.6 mm; medial/lateral, 1.5 mm). A 10 μL Hamilton syringe was then used to deliver the nanoparticle transducer (100 μg/mL, 10 μL) to the lateral ventricle at a depth of 1.7 mm from the dura. The injection was made at 1 μL/min, and the Hamilton syringe was kept in the injection site for an additional 5 to 10 min after injecting to ensure that all of the materials were infused. The burr hole was occluded with bone wax to prevent the leakage of cerebrospinal fluid. After that, the nanoparticle transducer (2 μL, 100 μg/mL) was injected subcutaneously at the dorsal site of each mouse. After 4 h, the mice were ready for the following whole-body optical imaging. The optical imaging of the two groups of mice was performed by an in vivo imaging system. The following experimental processes were the same as the in vivo glucose monitoring experimental processes.

RESULTS AND DISCUSSION

Preparation and Characterizations of the Nanoparticle Transducer. The nanoparticles were prepared using a reprecipitation method.[39] The nanoparticles consisted of polystyrene, the polymer PSMA, Nile Red, and the oxygen-sensitive dye PtOEPK. We used Nile Red and PtOEPK co-doped polystyrene nanoparticles to construct an FRET pair, where energy transfer occurs from Nile Red to PtOEPK, and finally obtained a ratiometric luminescent oxygen sensor. The glucose detection mechanism relies on the luminescent oxygen sensor integrated with GOx.[26,27] At an optimal doping concentration, the Nile Red dye exhibited a constant red emission at 650 nm, and PtOEPK exhibited a narrow phosphorescence peak at 760 nm, which was highly sensitive to the oxygen concentration. During the formation of polymer nanoparticles, the anhydride of PSMA was hydrolyzed and provided carboxyl groups on the surface of the nanoparticles (Scheme 1a). The surface carboxyl groups of the nanoparticles enabled subsequent conjugation with GOx and the catalase enzyme. In the presence of glucose, the oxygen reservoir around the nanoparticles was depleted because of the GOx-

https://doi.org/10.1021/acs.analchem.2c02600
Anal. Chem. 2022, 94, 14265−14272

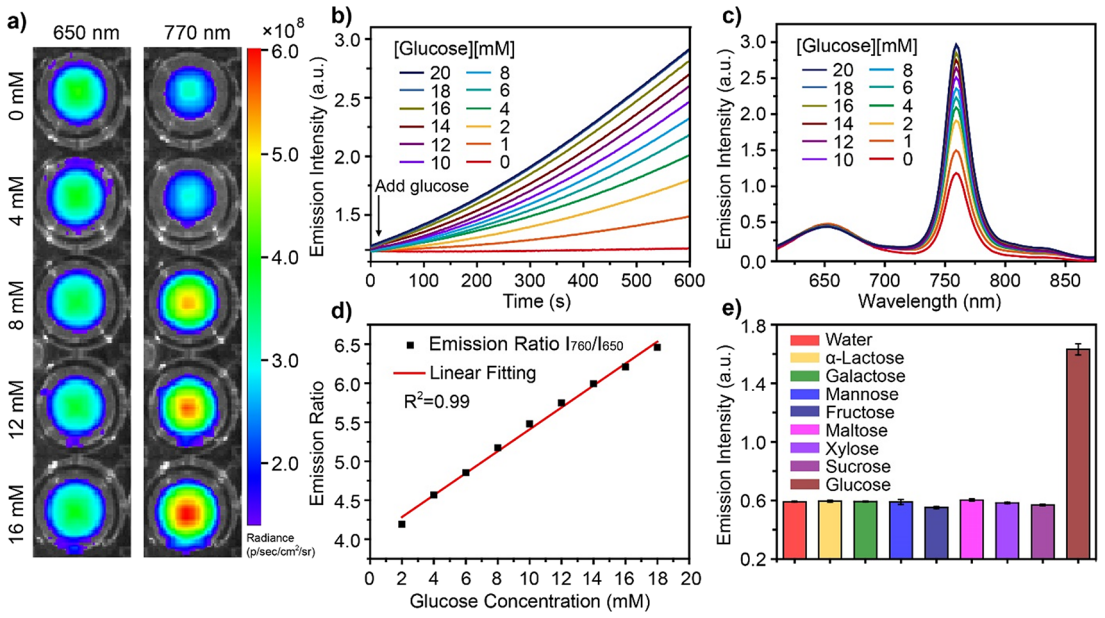

Figure 2. Optical properties of the nanoparticle transducer in vitro. (a) In vitro optical images of nanoparticle transducer at different glucose concentrations. (b) Glucose response curves of the nanoparticle transducer at 760 nm. (c) Emission spectra of the nanoparticle transducer in H_2O at different glucose concentrations. (d) Ratiometric calibration plot (I_{760}/I_{650}) as a function of glucose concentration. (e) Emission intensities after adding various carbohydrate analytes into the transducer solution. The concentration of each carbohydrate analyte was 20 mM.

catalyzed glucose oxidation reaction. Thus, the nanoparticle transducer can transform oxygen to a luminescence signal in the presence of glucose. The spatial and temporal changes in oxygen diffusion caused by glucose enzymatic reactions were simulated in a cuvette configuration and subcutaneous tissues, suggesting the reliable and robust glucose sensing property of the nanoparticle transducer in live mice.[26] Since the cerebral glucose metabolic characteristics were different between a normal brain and a neoplastic brain, the glucose transducer can potentially detect and quantify the cerebral glucose uptake rate in living mice (Scheme 1b).

The polymer nanoparticles were spherical and monodispersed in morphology, as shown by the transmission electron microscopy (TEM) image (Figure 1a). Dynamic light scattering (DLS) analyses indicated that the nanoparticles had an average hydrodynamic diameter of ∼17 nm. After GOx conjugation, the hydrodynamic diameter of the nanoparticle transducer increased to ∼19 nm (Figure 1b). The DLS and TEM characterizations confirmed the monodispersed size distribution and successful conjugation of the enzyme on the nanoparticle surface (Figure S1). The average surface ζ potentials of the nanoparticles and nanoparticle transducer were −35 and −20.6 mV, indicating their good colloidal stability in aqueous solutions (Figure S2).

We used optical spectroscopy to characterize the energy transfer in the dye-doped polymer nanoparticles. Figure 1c shows the absorption and the luminescence spectra of Nile Red and PtOEPK. The emission spectrum of Nile Red and the absorption spectrum of PtOEPK show an obvious overlap. The Förster radius from the donor and the acceptor was calculated to be ∼2 nm, suggesting that energy transfer occurred from Nile Red to PtOEPK. The quantum yield measurement of Nile Red in the nanoparticles and the parameters for calculation are shown in Figure S3 and Table S1, respectively. We prepared polymer nanoparticles with a constant Nile Red concentration (5 wt %) and varied PtOEPK concentrations (0−10 wt %). Figure 1d shows the luminescence spectra of the polymer nanoparticles in an air-saturated solution by using 560 nm excitation. As expected, the fluorescence intensity of Nile Red was quenched gradually, while the phosphorescence intensity of PtOEPK apparently increased with an increasing doping ratio of PtOEPK. At the optimal doping concentration (5 wt % Nile Red, 10 wt % PtOEPK), the nanoparticles exhibited an NIR emission quantum yield (∼1%) in the air-saturated solution (Figure S3c,d). The absorption spectra of the polymer nanoparticles with a constant Nile Red concentration and varied PtOEPK concentrations are shown in Figure S4. As indicated, the polymer nanoparticles can be excited by a 600 nm light source, which is important for in vivo imaging experiments to achieve deep tissue penetration. Because luminescence measurements from subcutaneous tissues could undergo spectral distortion,[40,41] we investigated the emission spectra of the transducer solution covered by mouse skin tissues (Figure S5), indicating minor spectral distortion in the wavelength range.

Glucose Sensing Properties in Vitro. We investigated the optical performance of the nanoparticle transducer to glucose variations. At the optimal doping fractions (5 wt % Nile Red, 10 wt % PtOEPK), the polymer nanoparticles exhibited a major absorption peak at ∼550 nm, a red emission peak at ∼650 nm, and an NIR phosphorescence peak at ∼760 nm. After enzyme bioconjugation, the aqueous solutions of the polymer nanoparticles were imaged at different glucose concentrations (Figure 2a). The NIR phosphorescence (∼760 nm) increased with the increasing glucose concentration, while the red emission (∼650 nm) from Nile Red remained constant. The constant red emission and the glucose-sensitive NIR emission constructed a ratiometric glucose sensing mechanism, which can be used for quantitative analysis of glucose concentrations. We characterized the luminescence response of the nanoparticle transducer. Upon addition of glucose to the transducer, the NIR emission intensity increased as the glucose oxidation reaction consumed oxygen (Figure 2b). The emission spectra at 600 s after glucose addition

https://doi.org/10.1021/acs.analchem.2c02600
Anal. Chem. 2022, 94, 14265−14272

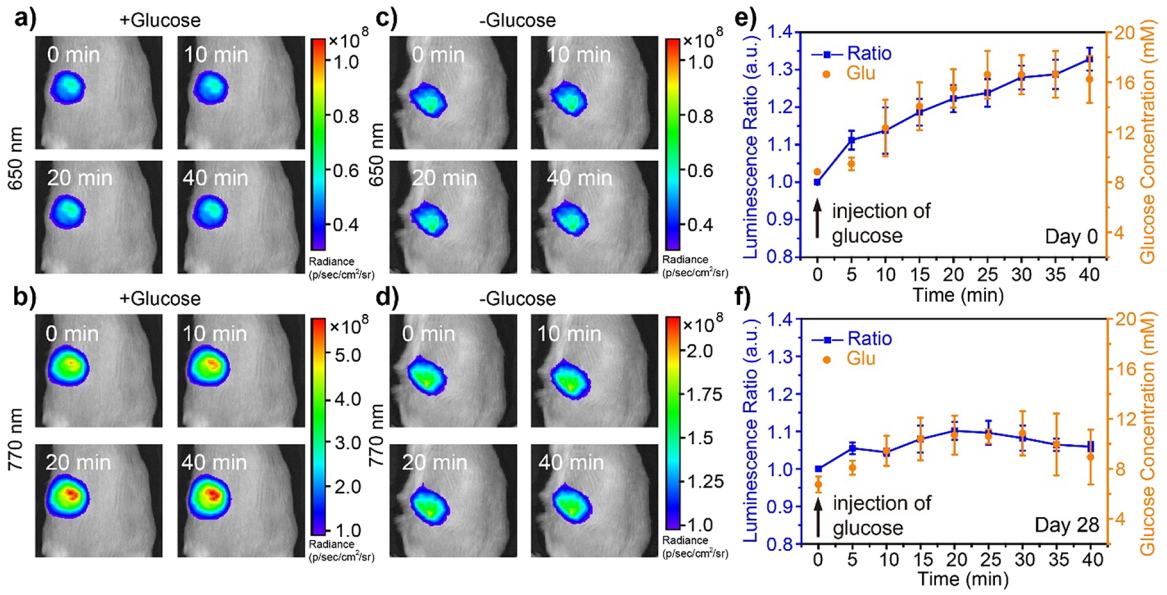

Figure 3. In vivo continuous glucose monitoring in mice. (a, b) Optical images of a BALB/C mouse with a subcutaneous nanoparticle transducer injection after glucose administration. (c, d) Optical images of a BALB/C mouse with a subcutaneous nanoparticle transducer injection and without glucose administration. (e, f) Luminescence ratios of two channels from the nanoparticle transducer after glucose administration and the corresponding glucose concentrations of the mice (0 and 28 days post-implantation).

display excellent sensitivity as glucose concentration varies from 2 to 18 mM. Then, the emission spectra were recorded at 600 s, clearly suggesting the ratiometric response of the nanoparticle transducer to different glucose concentrations (Figure 2c). Spectral characterizations also indicated that glucose does not affect the absorption and only increase the NIR emission of the nanoparticle transducer (Figures S6 and S7). The ratio of the emission peaks from 760 to 650 nm showed a linear relationship at the physiological glucose concentration (Figure 2d). The sensitivity of the glucose transducer was defined as the slope of the linear curve. When the glucose concentration increased by 1 mM, the emission ratio of the nanoparticle transducer increased by 8.3%, demonstrating its excellent sensitivity for glucose measurement. In addition, the glucose transducer showed high selectivity against other carbohydrates owing to the high specificity of the GOx enzyme toward glucose (Figure 2e).

In Vivo Continuous Glucose Monitoring of the Nanoparticle Transducer. We investigated the biocompatibility of the nanoparticles and nanoparticle transducer in several cell lines by MTT assays. As indicated in Figure S8, the polymer nanoparticles (100 μg/mL) showed negligible cytotoxicity in HeLa, U87, and BSC-1 cells. However, GOx alone can have cytotoxicity because the GOx-catalyzed reaction generates hydrogen peroxide. To solve this problem, catalase was also conjugated to the nanoparticle transducer to quickly decompose hydrogen peroxide. As a result, the nanoparticle transducer showed minimal cytotoxicity. Additional experiments indicated that catalase indeed improved the biocompatibility of the nanoparticle transducer in different conditions and had little effect on the luminescence spectra of the nanoparticle transducer (Figures S9–S11). In our previous study, the stability of the nanoparticle transducer can be enhanced by introducing catalase into the GOx-catalyzed reaction system.[28] In addition, we verified that the nanoparticle transducer generated negligible reactive oxygen species at a light dose of 30 J/cm^2 (Figure S12).

Next, the glucose response of the nanoparticle transducer was examined by an in vivo imaging system. The nanoparticle transducer was injected into each mouse subcutaneously. A hyperglycemia mouse model was managed by infusion of a glucose solution intraperitoneally. We performed two-channel optical imaging and calculated the ratio of the NIR phosphorescence intensity relative to the red luminescence intensity. Figure 3a,b shows the optical imaging of the mice with glucose injections from the red channel and NIR channel, respectively. As indicated, the phosphorescence intensities from the NIR channel in the mice with a nanoparticle transducer injection increased apparently with an increasing blood glucose level, while those from the red channel remained unchanged. In contrast, the luminescence signal from both the red and NIR channels remained constant for the mice without glucose administration (Figure 3c,d). The intensity ratios from the two channels were calculated and correlated with the blood glucose levels for mice in both the experimental group and control group. As shown in Figure 3e and Figure S13, the luminescence ratios in the mice from the experimental group closely tracked the increase in glucose level while the ratios in the mice from the control group remained constant, indicating the specific glucose response of the nanoparticle transducer in vivo. The long-term continuous glucose monitoring results were obtained 4 weeks post-injection of the nanoparticle transducer (Figure 3f and Figure S14). As indicated, the intensity ratios of the two channels closely tracked with the increasing blood glucose concentrations. The mice were treated with the same dose of glucose; therefore, the blood glucose level increased less at day 28 than that at day 0, likely due to the growth of the mice. A moderate decrease in sensitivity was observed for the monitoring results after 2 weeks, likely due to GOx degradation. Nevertheless, these results confirmed the reliable luminescence response of the nanoparticle transducer for long-term continuous glucose monitoring.

https://doi.org/10.1021/acs.analchem.2c02600
Anal. Chem. 2022, 94, 14265−14272

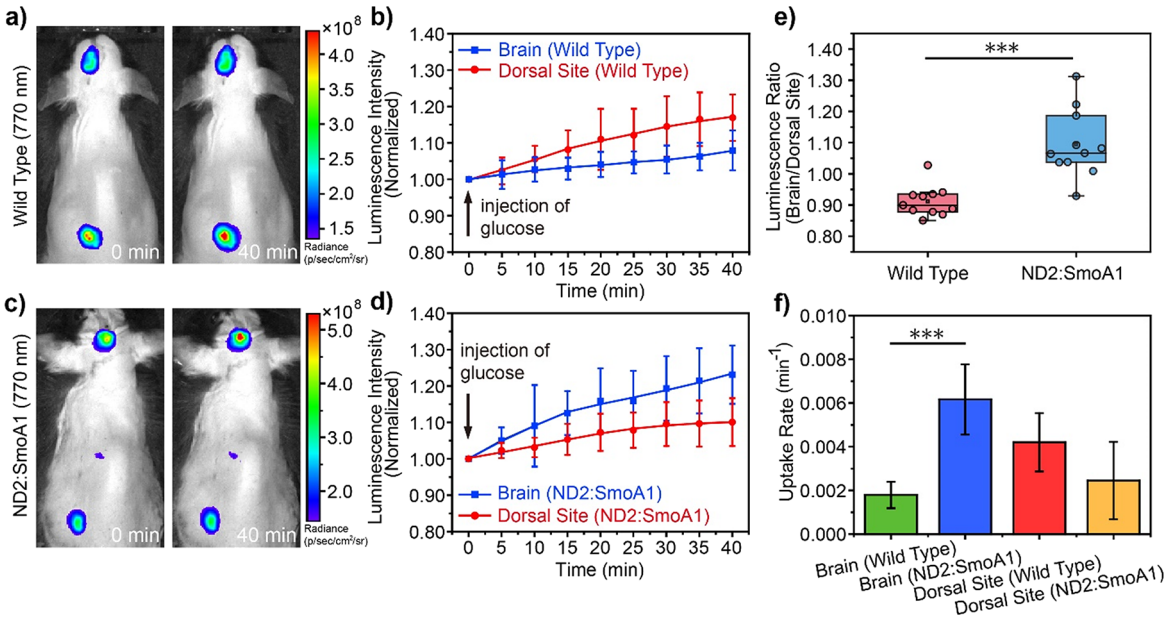

Figure 4. Dynamic imaging of cerebrospinal fluid glucose in wild-type mice and ND2:SmoA1 mice. (a, c) Optical images of a wild-type mouse and an ND2:SmoA1 mouse with the nanoparticle transducer implanted in the brain and dorsal site followed by glucose administration, respectively. (b, d) Averages and standard deviations of the normalized luminescence intensity from the brain and dorsal site in the two types of mice after glucose administration, respectively. (e) Ratios of the normalized luminescence intensities from the brain and dorsal site in the two types of mice at 40 min after glucose administration. The ratios were analyzed by a two-sided Student's *t* test. Significance levels: $***p < 0.001$. (f) Comparison of the fitted glucose uptake rates between wild-type and ND2:SmoA1 mice. Significance levels: $***p < 0.001$. All of the error bars represent the standard deviations.

Monitoring of Cerebrospinal Fluid Glucose Using the Nanoparticle Transducer. Cancer cells have an elevated glucose uptake compared with normal cells, which is a phenomenon called the Warburg effect.[42] Similarly, brain cancer cells require a higher glucose flux as compared to normal brain cells. It is important to develop a strategy for imaging glucose uptake in the brain and distinguish the different metabolic characteristics. Here, we attempted to explore cerebral metabolic abnormalities using the nanoparticle transducer. We chose a transgenic model named ND2:SmoA1, a mouse brain tumor model that is very similar to human medulloblastoma. Because it takes 2−4 months for ND2:SmoA1 mice to develop brain tumors, the ND2:SmoA1 mice in our experiments were likely at different stages of cancer development. Therefore, we used 11 ND2:SmoA1 mice and 11 wild-type C57BL/6 mice to investigate the cerebral glucose uptake. By a through-skull injection, the nanoparticle transducer was implanted into the lateral ventricle of the mouse brain, where the cerebrospinal fluid (CSF) circulates. CSF analysis, including the CSF glucose test, is useful in various severe neurological diseases and enables rapid diagnosis of brain diseases, such as meningitis,[43,44] Alzheimer's disease,[45] and neurosyphilis.[46] As a control, a dose of the nanoparticle transducer was implanted into the subcutaneous tissue of the dorsal site of each animal. After 4 h, a glucose solution was intraperitoneally injected into each mouse, and optical images and glucose measurements were acquired.

Figure 4a shows the NIR optical imaging of the wild-type mice after glucose treatment. As indicated, the intensity at the dorsal site showed an obvious increase, while the signal from the brain showed only a slight increase. This observation is consistent with the clinical results that the glucose concentration in the CSF is proportional to the glucose concentration in the blood and corresponds to 60−70% of that in blood.[47−49] The CSF glucose concentration and the CSF/blood glucose ratio are important for the differential diagnosis of many neurological disorders. However, hourly analysis of CSF glucose showed large diurnal fluctuations in the CSF/blood glucose ratio, which is closely related to food intake.[50] To circumvent this issue, we normalized the time-dependent luminescence intensities relative to the initial intensity immediately after glucose injection and used the intensity change curve at 40 min to evaluate glucose uptake. Figure 4b shows the normalized intensity changes of the brain and the dorsal site of the wild-type mice after glucose administration. Because the luminescence at both sites increased approximately linearly in the first 20 min, the intensity curves were linearly fitted, where the slope was defined as the glucose uptake rate. As indicated, the glucose uptake rate at the dorsal site was apparently higher than that at the brain site in the wild-type mice.

Optical imaging was further performed on the ND2:SmoA1 mice with brain tumor upon glucose administration (Figure 4c). The normalized time-dependent intensity changes from both the dorsal site and the brain are shown in Figure 4d. It is clear that the glucose uptake rate in the brain was higher than that in the dorsal site, suggesting the distinctive dynamics of cerebral glucose uptake in the ND2:SmoA1 mice. In contrast with the wild-type mice, the time-dependent intensity changes of the brain relative to those of the dorsal site in the ND2:SmoA1 mice exhibited an opposite trend, likely due to the abnormal glucose metabolism in the neoplastic brain. As for the CSF/blood glucose ratio, we used the luminescence intensity ratio of the brain relative to that of the dorsal site (40 min post glucose injection) as a reference value to distinguish the ND2:SmoA1 mice from the wild-type mice. The intensity ratios between the brain and the dorsal site from the ND2:SmoA1 mice showed significant differences from those

https://doi.org/10.1021/acs.analchem.2c02600
Anal. Chem. 2022, 94, 14265−14272

of the wild-type mice (Figure 4e). Specifically, most of the luminescence intensity ratios from the tumor-bearing mice were larger than 1, while those in the wild-type mice were less than 1. These results demonstrated the potential of this method in clinical brain tumor diagnosis.

Finally, we assessed the glucose uptake rates in the dorsal site and brain from both the wild-type and ND2:SmoA1 mice (Figure 4f). As indicated, the cerebral glucose uptake rate in the wild-type mice was significantly lower than that of the dorsal site. In contrast, the glucose uptake rate in the brain from the ND2:SmoA1 mice was much higher than that in the dorsal site. Notably, the cerebral glucose uptake rate of the ND2:SmoA1 mice was apparently higher than the glucose uptake rate in the normal mice, indicating that the cerebral glucose uptake rate could be an important indicator for brain tumor diagnosis. These results indicated that the nanoparticle glucose transducer is a promising optical tool for studying glucose metabolism in the mouse brain. For the possible accumulation effects and nanoparticle clearance, prior studies have shown that rigid conjugated polymer nanoparticles are biodegradable.[51,52] We are making efforts to develop biocompatible platforms that can maintain robust glucose measurement for a period of time and degrade in vivo after use.

CONCLUSIONS

In summary, we demonstrated that the NIR optical glucose transducer is a useful tool for quantifying glucose concentration and cerebral glucose uptake in living mice. We constructed a ratiometric luminescent oxygen-sensitive probe by using energy transfer from the Nile Red donor to the PtOEPK acceptor in polymer nanoparticles. After enzyme bioconjugation, the nanoparticle transducer exhibited highly sensitive NIR phosphorescence to glucose concentration, enabling continuous glucose monitoring and through-skull imaging of cerebral glucose uptake in vivo. By a through-skull injection to the lateral ventricle, we observed higher cerebral glucose uptake rates in ND2:SmoA1 mice comparing with those in wild-type mice, indicating the distinctive cerebral glucose uptake characteristics in mice bearing brain tumors. The NIR emission of the optical transducer exhibited deep penetration for imaging of cerebral glucose, providing the ability to detect glucose uptake without the use of radioactive tracers. As compared to bioluminescent and fluorescent glucose analogues, the nanoparticle transducer enables sensitive and reversible measurement of glucose. Because glucose is the primary energy source for most organisms, this transducer can be further used in the diagnosis of a variety of metabolic diseases with altered glucose metabolism.

ASSOCIATED CONTENT

Supporting Information

The Supporting Information is available free of charge at https://pubs.acs.org/doi/10.1021/acs.analchem.2c02600.

Materials, characterization, determination of fluorescence quantum yield, calculation of the Förster radius, spectroscopic properties, cytotoxicity, and animal studies of in vivo imaging used in this work (PDF)

AUTHOR INFORMATION

Corresponding Author

Changfeng Wu − *Department of Biomedical Engineering, Southern University of Science and Technology, Shenzhen 518055, China;* orcid.org/0000-0001-6797-9784; Email: wucf@sustech.edu.cn

Authors

Siyang Liu − *Harbin Institute of Technology, Harbin 150001, China; Department of Biomedical Engineering, Southern University of Science and Technology, Shenzhen 518055, China*

Ye Liu − *Department of Biomedical Engineering, Southern University of Science and Technology, Shenzhen 518055, China*

Zhe Zhang − *Department of Biomedical Engineering, Southern University of Science and Technology, Shenzhen 518055, China;* orcid.org/0000-0002-4144-6733

Xiaodong Wang − *Department of Biomedical Engineering, Southern University of Science and Technology, Shenzhen 518055, China*

Yicheng Yang − *Department of Biomedical Engineering, Southern University of Science and Technology, Shenzhen 518055, China*

Kai Sun − *Department of Chemistry and Bioengineering, University of Washington, Seattle, Washington 98195, United States;* orcid.org/0000-0002-1109-8934

Jiangbo Yu − *Department of Chemistry and Bioengineering, University of Washington, Seattle, Washington 98195, United States*

Daniel T. Chiu − *Department of Chemistry and Bioengineering, University of Washington, Seattle, Washington 98195, United States*

Complete contact information is available at: https://pubs.acs.org/10.1021/acs.analchem.2c02600

Author Contributions

All authors have given approval to the final version of the manuscript.

Notes

The authors declare no competing financial interest.

ACKNOWLEDGMENTS

This work was financially supported by the National Key R&D Program of China (Grant No. 2020YFA0909000), the Shenzhen Science and Technology Program (Grant Nos. KQTD20170810111314625 and JCYJ20210324115807021), and the Shenzhen Bay Laboratory (SZBL2021080601002).

REFERENCES

(1) Hay, N. *Nat. Rev. Cancer* **2016**, *16*, 635−649.
(2) Chang, C. H.; Pearce, E. L. *Nat. Immunol.* **2016**, *17*, 364−368.
(3) Momcilovic, M.; Shackelford, D. B. *Biomol. Ther.* **2018**, *26*, 81−92.
(4) Szablewski, L. *J. Alzheimer's Dis.* **2017**, *55*, 1307−1320.
(5) Wilding, J. P. H. *Metab., Clin. Exp.* **2014**, *63*, 1228−1237.
(6) Zierler, K. *Am. J. Physiol.* **1999**, *276*, E409−E426.
(7) Conti, P. S. *Cancer Invest.* **1995**, *13*, 244−259.
(8) Kelloff, G.; Hoffman, J. M.; Johnson, B.; Scher, H. I.; Siegel, B. A.; Cheng, E. Y.; Cheson, B. D.; O'Shaughnessy, J.; Guyton, K. Z.; Mankoff, D. A.; Shankar, L.; Larson, S. M.; Sigman, C. C.; Schilsky, R. L.; Sullivan, D. C. *Clin. Cancer Res.* **2005**, *11*, 2785−2808.
(9) Ben-Haim, S.; Ell, P. *J. Nucl. Med.* **2009**, *50*, 88−99.
(10) Nordberg, A.; Rinne, J. O.; Kadir, A.; Langstrom, B. *Nat. Rev. Neurol.* **2010**, *6*, 78−87.
(11) Vallabhajosula, S.; Solnes, L.; Vallabhajosula, B. *Semin. Nucl. Med.* **2011**, *41*, 246−264.

(12) Roslin, M.; Henriksson, R.; Bergstrom, P.; Ungerstedt, U.; Bergenheim, A. T. *J. Neuro-Oncol.* **2003**, *61*, 151−160.
(13) Walker-Samuel, S.; Ramasawmy, R.; Torrealdea, F.; Rega, M.; Rajkumar, V.; Johnson, S. P.; Richardson, S.; Goncalves, M.; Parkes, H. G.; Arstad, E.; Thomas, D. L.; Pedley, R. B.; Lythgoe, M. F.; Golay, X. *Nat. Med.* **2013**, *19*, 1067−1072.
(14) Nasrallah, F. A.; Pages, G.; Kuchel, P. W.; Golay, X.; Chuang, K. H. *J. Cereb. Blood Flow Metab.* **2013**, *33*, 1270−1278.
(15) Jin, T.; Mehrens, H.; Wang, P.; Kim, S. G. *NeuroImage* **2016**, *143*, 82−90.
(16) Huang, J. P.; van Zijl, P. C. M.; Han, X. Q.; Dong, C. M.; Cheng, G. W. Y.; Tse, K. H.; Knutsson, L.; Chen, L.; Lai, J. H. C.; Wu, E. X.; Xu, J. D.; Chan, K. W. Y. *Sci. Adv.* **2020**, *6*, eaba3884.
(17) Wolfbeis, O. S.; Oehme, I.; Papkovskaya, N.; Klimant, I. *Biosens. Bioelectron.* **2000**, *15*, 69−76.
(18) Wu, S.; Kong, X. J.; Cen, Y.; Yuan, J.; Yu, R. Q.; Chu, X. *Nanoscale* **2016**, *8*, 8939−8946.
(19) Li, N.; Than, A.; Wang, X. W.; Xu, S. H.; Sun, L.; Duan, H. W.; Xu, C. J.; Chen, P. *ACS Nano* **2016**, *10*, 3622−3629.
(20) Ma, J. L.; Yin, B. C.; Wu, X.; Ye, B. C. *Anal. Chem.* **2017**, *89*, 1323−1328.
(21) Wang, H.; Yi, J. H.; Yu, Y. Y.; Zhou, S. Q. *Nanoscale* **2017**, *9*, 509−516.
(22) Akkaya, I.; Selim, E.; Altintas, M.; Engin, M. *J. Innovative Opt. Health Sci.* **2018**, *11*, 1850035.
(23) Shibata, H.; Heo, Y. J.; Okitsu, T.; Matsunaga, Y.; Kawanishi, T.; Takeuchi, S. *Proc. Natl. Acad. Sci. U. S. A.* **2010**, *107*, 17894−17898.
(24) Heo, Y. J.; Shibata, H.; Okitsu, T.; Kawanishi, T.; Takeuchi, S. *Proc. Natl. Acad. Sci. U. S. A.* **2011**, *108*, 13399−13403.
(25) Maric, T.; Mikhaylov, G.; Khodakivskyi, P.; Bazhin, A.; Sinisi, R.; Bonhoure, N.; Yevtodiyenko, A.; Jones, A.; Muhunthan, V.; Abdelhady, G.; Shackelford, D.; Goun, E. *Nat. Methods* **2019**, *16*, 526−532.
(26) Sun, K.; Tang, Y.; Li, Q.; Yin, S. Y.; Qin, W. P.; Yu, J. B.; Chiu, D. T.; Liu, Y. B.; Yuan, Z.; Zhang, X. J.; Wu, C. F. *ACS Nano* **2016**, *10*, 6769−6781.
(27) Sun, K.; Yang, Y. K.; Zhou, H.; Yin, S. Y.; Qin, W. P.; Yu, J. B.; Chiu, D. T.; Yuan, Z.; Zhang, X. J.; Wu, C. F. *ACS Nano* **2018**, *12*, 5176−5184.
(28) Sun, K.; Ding, Z. Y.; Zhang, J. C.; Chen, H. B.; Qin, Y. L.; Xu, S. H.; Wu, C. F.; Yu, J. B.; Chiu, D. T. *Adv. Healthcare Mater.* **2021**, *10*, 2001019.
(29) Sun, K.; Liu, S. Y.; Liu, J.; Ding, Z. Y.; Jiang, Y. F.; Zhang, J. C.; Chen, H. B.; Yu, J. B.; Wu, C. F.; Chiu, D. T. *Anal. Chem.* **2021**, *93*, 2359−2366.
(30) Liu, J.; Fang, X. F.; Zhang, Z.; Liu, Z. H.; Liu, J.; Sun, K.; Yuan, Z.; Yu, J. B.; Chiu, D. T.; Wu, C. F. *Anal. Chem.* **2022**, *94*, 2195−2203.
(31) Lundgaard, I.; Li, B.; Xie, L.; Kang, H.; Sanggaard, S.; Haswell, J. D.; Sun, W.; Goldman, S.; Blekot, S.; Nielsen, M.; Takano, T.; Deane, R.; Nedergaard, M. *Nat. Commun.* **2015**, *6*, 1−12.
(32) Flavahan, W. A.; Wu, Q. L.; Hitomi, M.; Rahim, N.; Kim, Y.; Sloan, A. E.; Weil, R. J.; Nakano, I.; Sarkaria, J. N.; Stringer, B. W.; Day, B. W.; Li, M. Z.; Lathia, J. D.; Rich, J. N.; Hjelmeland, A. B. *Nat. Neurosci.* **2013**, *16*, 1373−1382.
(33) Cunnane, S. C.; Trushina, E.; Morland, C.; Prigione, A.; Casadesus, G.; Andrews, Z. B.; Beal, M. F.; Bergersen, L. H.; Brinton, R. D.; de la Monte, S.; Eckert, A.; Harvey, J.; Jeggo, R.; Jhamandas, J. H.; Kann, O.; la Cour, C. M.; Martin, W. F.; Mithieux, G.; Moreira, P. I.; Murphy, M. P.; Nave, K. A.; Nuriel, T.; Oliet, S. H. R.; Saudou, F.; Mattson, M. P.; Swerdlow, R. H.; Millan, M. J. *Nat. Rev. Drug Discovery* **2020**, *19*, 609−633.
(34) Tu, T. W.; Ibrahim, W. G.; Jikaria, N.; Munasinghe, J. P.; Witko, J. A.; Hammoud, D. A.; Frank, J. A. *Sci. Rep.* **2018**, *8*, 1−12.
(35) Lozano, A.; Franchi, F.; Seastres, R. J.; Oddo, M.; Lheureux, O.; Badenes, R.; Scolletta, S.; Vincent, J. L.; Creteur, J.; Taccone, F. S. *J. Neurosurg. Anesth.* **2020**, *32*, 162−169.
(36) Greco, T.; Vespa, P. M.; Prins, M. L. *Exp. Neurol.* **2020**, *329*, 113289.
(37) Bergsneider, M.; Hovda, D. A.; Shalmon, E.; Kelly, D. F.; Vespa, P. M.; Martin, N. A.; Phelps, M. E.; McArthur, D. L.; Caron, M. J.; Kraus, J. F.; Baker, D. P. *J. Neurosurg.* **1997**, *86*, 241−251.
(38) Frykholm, P.; Hillered, L.; Långström, B.; Persson, L.; Valtysson, J.; Enblad, P. *J. Neurosurg.* **2005**, *102*, 1076−1084.
(39) Wu, C. F.; Bull, B.; Christensen, K.; McNeill, J. *Angew. Chem., Int. Ed.* **2009**, *48*, 2741−2745.
(40) Shen, Y. L.; Lifante, J.; Fernández, N.; Jaque, D.; Ximendes, E. *ACS Nano* **2020**, *14*, 4122−4133.
(41) Shen, Y. L.; Lifante, J.; Zabala-Gutierrez, I.; de la Fuente-Fernández, M.; Granado, M.; Fernández, N.; Rubio-Retama, J.; Jaque, D.; Marin, R.; Ximendes, E.; Benayas, A. *Adv. Mater.* **2021**, *34*, 2107764.
(42) Heiden, M. G. V.; Cantley, L. C.; Thompson, C. B. *Science* **2009**, *324*, 1029−1033.
(43) Spanos, A.; Harrell, F. E.; Durack, D. T. *JAMA, J. Am. Med. Assoc.* **1989**, *262*, 2700−2707.
(44) Bonsu, B. K.; Harper, M. B. *Pediatr. Infect. Dis. J.* **2004**, *23*, 511−517.
(45) Pappas, C.; Klinedinst, B. S.; Le, S.; Wang, Q.; Larsen, B.; McLimans, K.; Lockhart, S. N.; Allenspach-Jorn, K.; Mochel, J. P.; Willette, A. A. *Alzheimer's Dementia* **2020**, *6*, No. e12080.
(46) Pastuszczak, M.; Wojas-Pelc, A.; Jaworek, A. *Open Med.* **2013**, *8*, 48−51.
(47) Nigrovic, L. E.; Kimia, A. A.; Shah, S. S.; Neuman, M. *N. Engl. J. Med.* **2012**, *366*, 576−578.
(48) Klepper, J.; Voit, T. *Eur. J. Pediatr.* **2002**, *161*, 295−304.
(49) Seehusen, D. A.; Reeves, M. M.; Fomin, D. A. *Am. Fam. Physician* **2003**, *68*, 1103−1108.
(50) Verbeek, M. M.; Leen, W. G.; Willemsen, M. A.; Slats, D.; Claassen, J. A. *J. Cereb. Blood Flow Metab.* **2016**, *36*, 899−902.
(51) Miao, Q. Q.; Xie, C.; Zhen, X.; Lyu, Y.; Duan, H. W.; Liu, X. G.; Jokerst, J. V.; Pu, K. Y. *Nat. Biotechnol.* **2017**, *35*, 1102−1110.
(52) Jiang, Y. Y.; Upputuri, P. K.; Xie, C.; Zeng, Z. L.; Sharma, A.; Zhen, X.; Li, J. C.; Huang, J. G.; Pramanik, M.; Pu, K. Y. *Adv. Mater.* **2019**, *31*, 1808166.

https://doi.org/10.1021/acs.analchem.2c02600
Anal. Chem. 2022, 94, 14265−14272